Journal of Functional Materials and Applied Engineering

Research Paper

Electrochemical Detection of Metronidazole Based on $MnMoO_4$g-C_3N_4 Modified Electrode

Liam O'Brien[1], Chloe Dubois[1,*], Sophia Rossi[2]

[1] University of Management and Technology, Lahore, Pakistan
[2] School of life science, University of Southampton, Southampton, SO17 1BJ, UK
*Corresponding author: Brien@umt.edu.pk; Chdubois@umt.edu.pk; Sophia00rossi@soton.ac.uk

Abstract. $MnMoO_4$/g-C_3N_4 nanocomposites were synthesized via a hydrothermal method. The morphology and structure of the composites were characterized by X-ray diffraction (XRD), Fourier transform infrared spectroscopy (FT-IR), and scanning electron microscopy (SEM). The $MnMoO_4$/g-C_3N_4 nanocomposite was coated onto the surface of a glassy carbon electrode (GCE) via a drop-coating method to construct an electrochemical sensor for the detection of metronidazole (MNZ). The electrochemical behavior of the $MnMoO_4$/g-C_3N_4/GCE electrode was investigated using cyclic voltammetry (CV) and differential pulse voltammetry (DPV). The effects of pH value and scan rate on the current response were examined. Under optimized conditions, the sensor exhibited a linear detection range for MNZ from 0.5 to 2400 μmol/L, with a limit of detection (LOD, 3σ/k) of 1.33 nmol/L. The sensor also demonstrated excellent selectivity, stability, and reproducibility. When applied to the detection of MNZ in egg and milk samples, the spiked recoveries ranged from 97.7% to 103.7% and 96.9% to 102.4%, respectively, with relative standard deviations (RSDs) of 1.1%–2.2%. These results indicate that the prepared $MnMoO_4$/g-C_3N_4/GCE sensor is viable for the detection of MNZ residues in real food samples, providing a novel approach for food safety supervision.

Keywords: *Manganese molybdate; Graphitic carbon nitride; Electrochemical detection; Metronidazole*

Received on 02 June 2025, Accepted on 02 August 2025, Published on 15 September 2025

1 Introduction

Metronidazole [1-(2-hydroxyethyl)-2-methyl-5-nitroimidazole, MNZ] is a broad-spectrum antimicrobial nitroimidazole derivative[1], widely used for the treatment of anaerobic infections and protozoal diseases[2]. It is particularly effective against hemorrhagic enteritis in livestock, histomoniasis, and trichomoniasis in poultry[3]. However, irrational or excessive use of MNZ can lead to its persistence in animal meat and liver. Ingestion through the food chain allows MNZ to accumulate in the human body, potentially causing various toxic reactions[4]. Due to its potential carcinogenicity, the National Food Safety Standard of China—Maximum Residue Limits for Veterinary Drugs in Foods (2019)—explicitly prohibits the detection of metronidazole in animal-derived foods[5]. Consequently, monitoring MNZ levels in animal-derived foods is of great significance for ensuring food quality and safety. Currently, common analytical methods for MNZ detection include high-performance liquid chromatography (HPLC)[6], liquid chromatography-tandem mass spectrometry (LC-MS/MS)[7], Raman spectroscopy[8], and fluorescence spectrophotometry[9]. Nevertheless, these methods suffer from drawbacks such as cumbersome sample pretreatment, lengthy analysis times, reliance on expensive instrumentation, and difficulties in rapid, on-site detection of drug residues[10]. In contrast, electrochemical analysis has garnered increasing attention from researchers due to its high sensitivity, simple instrumentation, ease of operation, and portability[11].

In recent years, researchers have developed various novel electrode modification materials to enhance the performance of electrochemical sensors. Among them, nanomaterials have attracted considerable interest

owing to their unique physicochemical properties and electrochemical performance. Diverse composite nanostructures can be fabricated by synthesizing bimetallic transition metal oxides—such as iron molybdate, zinc molybdate, yttrium molybdate, and manganese molybdate—via different synthetic techniques[12–13]. Their multivalent states facilitate redox reactions. Manganese molybdate ($MnMoO_4$) offers advantages such as high chemical stability and low cost; however, its poor electrical conductivity limits its practical electrochemical applications. Consequently, doping and other modification strategies are often employed to improve its performance[14–15]. Selvi et al.[16] prepared a flower-like Mn/SnO@rGO nanocomposite-modified electrode via hydrothermal and ultrasonication methods. This electrode enhanced the current response toward 2-methyl-5-nitroimidazole (Dimetridazole, DMZ), featuring a low detection limit, wide linear range, and good selectivity, rendering it suitable for detecting DMZ in contaminated water, milk, and egg samples.

Graphitic carbon nitride (g-C_3N_4) is a polymeric material with a graphite-like stacked two-dimensional layered structure[17]. It possesses merits such as good biocompatibility, high stability, and a large specific surface area[18–20], and has been utilized as an environmental catalyst and electrode modifier for pollutant degradation and detection[21–24]. Studies indicate that modifying g-C_3N_4 with other semiconductors can enhance its catalytic activity[25]. Anupriya et al.[26] synthesized an Sg-C_3N_4/$CuWO_4$ nanocomposite-modified electrode via a simple ultrasonication method for the electrochemical detection of nitrofurazone (NZ). This sensor exhibited excellent performance for NZ detection within a concentration range of 0.005–877 μmol/L, with a detection limit of 3.0 nmol/L, along with outstanding stability, repeatability, and reproducibility. Ahmad et al.[27] constructed a novel MoS_2/g-C_3N_4 composite-modified electrode via a hydrothermal method for the electrochemical detection of MNZ. This sensor offered advantages including a wide linear range (2–125 μmol/L), low detection limit (0.099 μmol/L), high sensitivity, and low cost, providing an effective method for monitoring MNZ in aquatic environments.

In this study, $MnMoO_4$/g-C_3N_4 nanocomposites were synthesized via a hydrothermal method, and their morphology and structure were thoroughly characterized. The composite was coated onto a GCE surface, and the electrochemical behavior of MNZ on this modified electrode, along with influencing factors, was investigated using CV and DPV. The constructed sensor exhibited a wide linear range (0.5–2400 μmol/L) and a low detection limit (1.33 nmol/L) for MNZ detection. When applied to egg and milk samples, the spiked recoveries ranged from 97.7% to 103.7% and 96.9% to 102.4%, respectively, offering a novel method for detecting MNZ residues in food.

2 Experimental Section

2.1 Instruments and Reagents

CHI 660E electrochemical workstation (Shanghai Chenhua Instrument Co., Ltd.); IRAffinity-1 Fourier transform infrared spectrometer and AXIS Nova X-ray photoelectron spectrometer (Shimadzu Corporation, Japan); HITACHI SU8600 scanning electron microscope (SEM) and HITACHI HT7800 transmission electron microscope (TEM) (Hitachi High-Tech Corporation, Japan); XRD-6100 X-ray diffractometer (Bruker Corporation, Germany); SXH-5-12LTP muffle furnace (Shanghai Yitian Scientific Instrument Co., Ltd.). A conventional three-electrode system was employed: a GCE (diameter: 3 mm) or modified GCE as the working electrode, a platinum wire as the counter electrode, and a saturated calomel electrode (SCE) as the reference electrode.

Urea (CH_4N_2O), $K_3[Fe(CN)_6]$/$K_4[Fe(CN)_6]$, $MnCl_2{\cdot}2H_2O$, $Na_2MoO_4{\cdot}2H_2O$, and MNZ were purchased from Shanghai Aladdin Biochemical Technology Co., Ltd. $Na_2HPO_4{\cdot}12H_2O$ and $NaH_2PO_4{\cdot}2H_2O$ were obtained from Tianjin Tianli Chemical Reagent Co., Ltd. All reagents were of analytical grade, and deionized water was used throughout the experiments.

2.2 Experimental Methods

2.2.1 Preparation of $MnMoO_4$/g-C_3N_4

Preparation of g-C_3N_4[28]: 10 g of urea was placed in a 50 mL covered alumina crucible and heated in a muffle furnace at 550 °C for 4 h, with a heating rate of 4 °C/min. After cooling to room temperature, the sample was collected and ground to obtain a yellow powder, identified as g-C_3N_4.

Preparation of $MnMoO_4$/g-C_3N_4 composites[29]: 20.0 mg of g-C_3N_4 was dissolved in 30 mL of deionized water, and 0.40 g of $MnCl_2 \cdot 4H_2O$ was added. The mixture was stirred rapidly for 1 h to obtain Solution A. Separately, 40.0 mmol of polyethylene glycol (PEG) and 0.48 g of $Na_2MoO_4 \cdot 2H_2O$ were mixed and stirred for 45 min to obtain Solution B. Solution B was slowly added to Solution A, and the mixture was stirred at room temperature for 1 h. The resulting mixture was transferred into a Teflon-lined autoclave and subjected to hydrothermal reaction at 200 °C for 5 h. After cooling to room temperature, the resulting $MnMoO_4$/g-C_3N_4 composite was washed sequentially three times with ethanol and water, and then dried for subsequent use.

2.2.2 Preparation of $MnMoO_4$/g-C_3N_4/GCE

The GCE was polished with alumina slurry on a polishing cloth to a mirror finish, followed by sequential ultrasonic cleaning in ethanol and deionized water. 5 mg of $MnMoO_4$/g-C_3N_4 was dispersed in 1 mL of deionized water and sonicated for 30 min. 5 µL of the $MnMoO_4$/g-C_3N_4 dispersion was evenly dropped onto the GCE surface and dried under an infrared lamp for 10 min to obtain the $MnMoO_4$/g-C_3N_4/GCE. For comparison, $MnMoO_4$/GCE, MnO_2/GCE, MoO_3/GCE, and g-C_3N_4/GCE were prepared using the same procedure; the preparation process is illustrated in Figure S1.

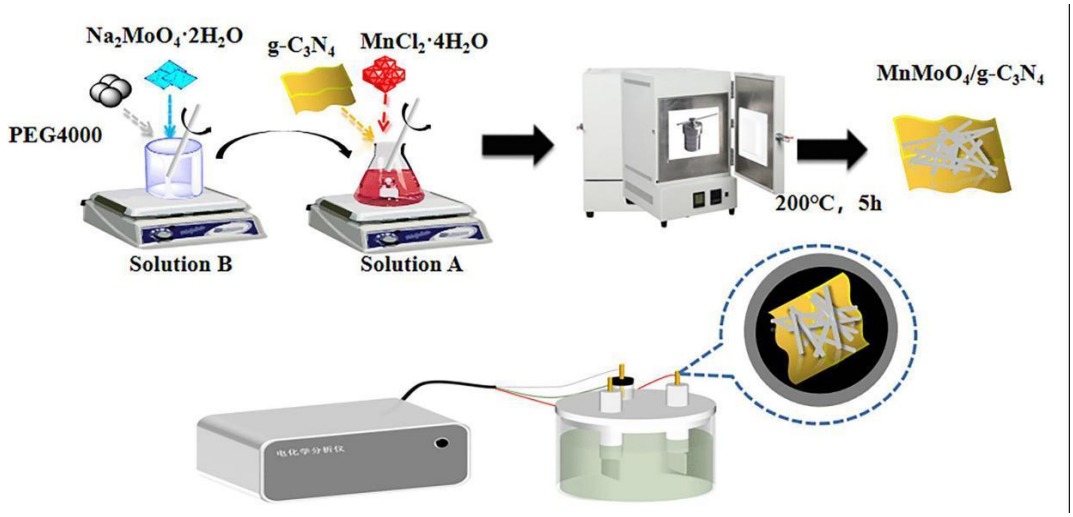

Figure S1. The preparation process of the MnMoO4/g-C3N4/GCE

2.2.3 Electrochemical Measurements

Electrochemical measurements were conducted in a standard three-electrode system: bare GCE, g-C_3N_4/GCE, $MnMoO_4$/GCE, or $MnMoO_4$/g-C_3N_4/GCE served as the working electrode, a platinum sheet as the counter electrode, and SCE as the reference electrode. Electrochemical impedance spectroscopy (EIS) and cyclic voltammetry (CV) were performed in a 0.1 mol/L KCl solution containing 5.0 mmol/L $K_3[Fe(CN)_6]$/$K_4[Fe(CN)_6]$. Appropriate volumes of MNZ standard solution were added to a phosphate buffer solution (PBS, 0.1 mol/L NaH_2PO_4–Na_2HPO_4, pH 7.0) for CV scanning. The scan rate was 100 mV/s, and the potential window ranged from −1.2 to 0.2 V. Differential pulse voltammetry (DPV) was performed with a potential scan range of −0.7 to −0.1 V, a pulse width of 0.1 s, a pulse period of 0.2 s, and an amplitude of 0.05 V. After each measurement, the electrode was scanned repeatedly in 0.1 mol/L PBS (pH 7.0) to renew the electrode surface. EIS was recorded over a frequency range of 0.01 Hz to 100 kHz with an amplitude of 0.005 V. All electrochemical tests were carried out at room temperature (25 °C). A 1.0 mmol/L MNZ standard solution was prepared by dissolving 0.0171 g of MNZ standard in deionized water and diluting to 100 mL in a volumetric flask. This stock solution was stored refrigerated and diluted with PBS to the desired concentration prior to use.

2.2.4 Real Sample Pretreatment

Eggs and milk were purchased from local supermarkets. For egg samples, the yolk and egg white were thoroughly homogenized. 2 mL of the homogenate was mixed with 8 mL of PBS (0.1 mol/L, pH 7.0) and shaken vigorously.

The mixture was centrifuged at 3000 r/min for 10 min. The supernatant was diluted tenfold with 0.1 mol/L PBS (pH 7.0) to obtain the test solution. For milk samples, the milk was centrifuged at 6000 r/min for 30 min. The supernatant was diluted tenfold with 0.1 mol/L PBS (pH 7.0) to obtain the test sample.

3 Results and Discussion

3.1 Material Characterization

The morphology and structure of the prepared materials were characterized by SEM. Figure 1A-a shows the SEM image of $MnMoO_4$, revealing a morphology consisting of nanorods and nanoparticles. The nanorods are approximately 400 nm in length, while the nanoparticles have a diameter of about 50 nm. Figures 1A-b and 1A-c present SEM images of the $MnMoO_4$/g-C_3N_4 composite at different magnifications. It is evident that the $MnMoO_4$ nanorods are uniformly distributed on the surface of g-C_3N_4 nanosheets. The energy-dispersive X-ray spectroscopy (EDS) spectrum of $MnMoO_4$/g-C_3N_4 (Figure S2G in ESI) confirms the presence of five elements: Mn, Mo, O, C, and N. The elemental mapping images (Figures S2A–S2F in ESI) demonstrate that Mn, Mo, O, C, and N are homogeneously distributed across the entire surface of the $MnMoO_4$/g-C_3N_4 composite, with no observable impurities. In the high-resolution transmission electron microscopy (HRTEM) image of $MnMoO_4$/g-C_3N_4 (Figure S2H in ESI), lattice fringes with spacings of 0.285 and 0.345 nm correspond to the (112) and (220) crystal planes of $MnMoO_4$[30–31], respectively, while the fringe spacing of 0.340 nm is attributed to the (002) plane of g-C_3N_4[32]. Figure 1B displays the X-ray diffraction (XRD) patterns of g-C_3N_4, $MnMoO_4$, and the $MnMoO_4$/g-C_3N_4 composite. Pure g-C_3N_4 exhibits two distinct characteristic peaks at 13.2° and 27.3°, corresponding to the (100) and (002) crystal planes of g-C_3N_4[33], which are ascribed to the in-plane structural ordering of triazine units and the interlayer stacking of aromatic systems in g-C_3N_4[34], respectively. In addition to the characteristic peaks of g-C_3N_4, distinct diffraction peaks corresponding to $MnMoO_4$ (JCPDS No. 78-0221) are observed in Figure 1C.

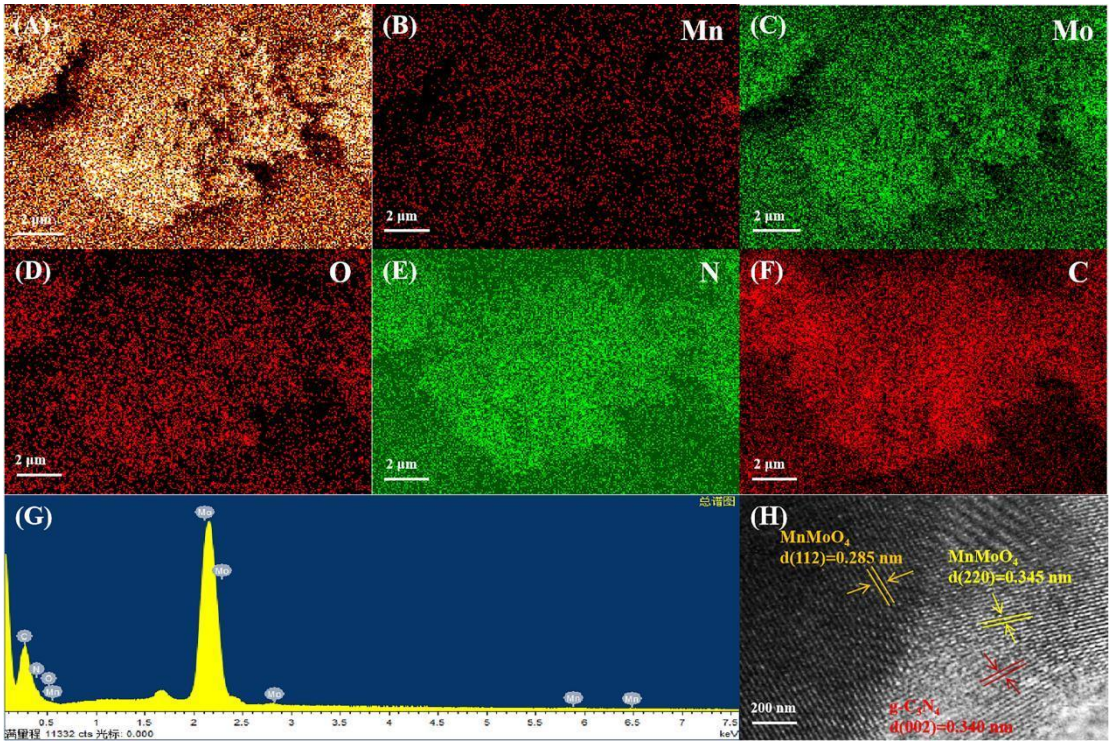

Figure S2 (A) The element mapping of MnMoO4/g-C3N4; (B) the Mn element; (C) the Mo element; (D) the O element; (E) the N element and (F) the C element ;(G) EDS spectrum of MnMoO4/g-C3N4; (H)The HRTEM image of MnMoO4/g-C3N4.

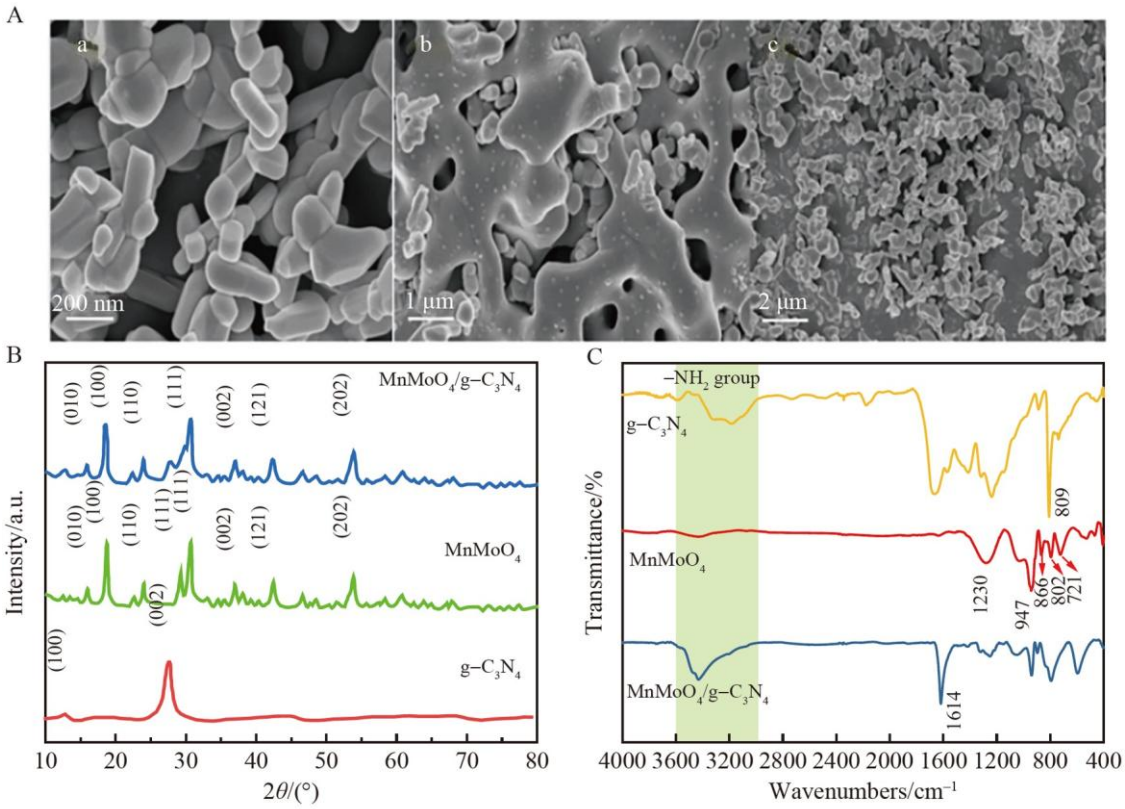

Figure 1 (A) Scanning electron microscopy images of MnMoO4 (a) and MnMoO4/g-C3N4 composites (b, c); (B) X-ray diffraction patterns and (C) Fourier transform infrared spectra of g-C3N4, MnMoO4 and MnMoO4/g-C3N4

Specifically, peaks at 15.8°, 18.8°, 24.1°, 29.6°, 36.7°, 42.4°, and 53.7° correspond to the (010), (100), (110), (111), (002), (121), and (202) crystal planes of $MnMoO_4$[35], respectively. Fourier transform infrared (FT-IR) spectroscopy was employed to investigate the structure and functional groups of g-C_3N_4, $MnMoO_4$, and the $MnMoO_4$/g-C_3N_4 nanocomposite (Figure 1C). The results indicate that the specific absorption band of g-C_3N_4 at 810 cm^{-1} is associated with the stretching of the s-triazine ring. Absorption peaks at 1573, 1408, 1330, and 1250 cm^{-1} correspond to the stretching vibrations of aromatic C–N bonds. The band at 1640 cm^{-1} is attributed to the stretching vibration of C=N. The broad absorption band in the range of 3100–3350 cm^{-1} corresponds to the vibrational modes of $–NH_2$ functional groups. In the FT-IR spectrum of $MnMoO_4$, the peak at 939 cm^{-1} corresponds to the stretching vibration of Mo=O. The peak at 897 cm^{-1} is assigned to the bending vibration of Mo–O–Mo, while peaks at 843 and 798 cm^{-1} are attributed to the stretching vibrations of the MoO_4 tetrahedron. The peak at 599 cm^{-1} corresponds to the Mo–O vibration of MoO_x[36]. In the FT-IR spectrum of the $MnMoO_4$/g-C_3N_4 composite, besides the characteristic peaks of $MnMoO_4$, a strong peak is observed in the range of 1200–1650 cm^{-1}, corresponding to the stretching vibration of aromatic C–N in g-C_3N_4, further confirming the successful preparation of the $MnMoO_4$/g-C_3N_4 composite. The X-ray photoelectron spectroscopy (XPS) survey spectrum of $MnMoO_4$/g-C_3N_4 (Figure S3A in ESI) reveals the presence of Mn, Mo, O, N, and C elements. In the C 1s XPS spectrum (Figure S3B in ESI), four peaks located at 283.28, 284.78, 285.32, and 286.82 eV correspond to C–Mn/C–Mo, C–C, C–N, and C–O bonds[37], respectively. The N 1s XPS spectrum (Figure S3C in ESI) shows peaks at 396.82 and 397.57 eV, attributed to the sp^2-hybridized nitrogen atoms of the triazine ring in g-C_3N_4, while a strong peak at 399.06 eV corresponds to N–$(C)_3$. In the O 1s spectrum (Figure S3D in ESI), two peaks at 529.94 and 531.73 eV correspond to Mn–O and O–H, respectively [38]. In the Mn 2p spectrum, two peaks near 641.5 and 653.3 eV are associated with Mn^{2+} $2p_3/_2$ and Mn^{2+} $2p_1/_2$ (Figure S3E in ESI). The Mo 3d spectrum (Figure S3F in ESI) displays characteristic peaks of Mo^{6+} $3d_5/_2$ and Mo^{6+} $3d_3/_2$ at 232.29 and 235.41 eV, respectively [39].

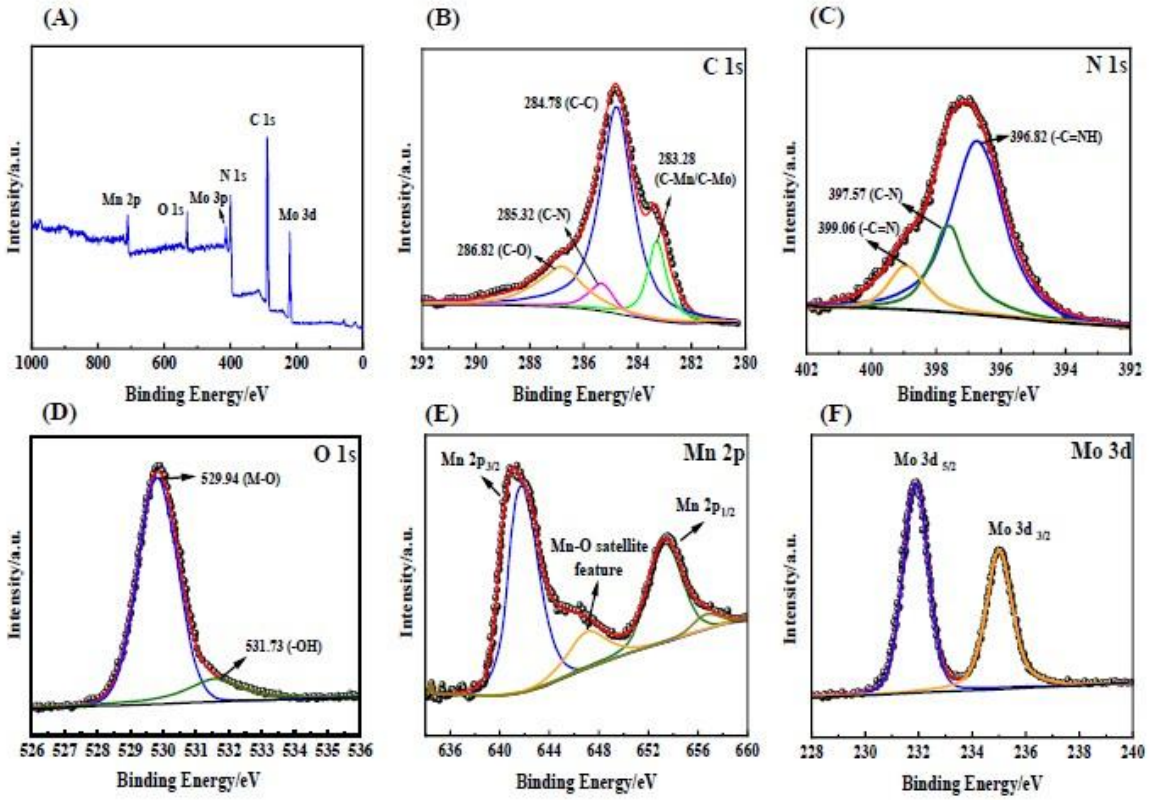

Figure.S3 X-ray photoelectron spectroscopy (XPS) patterns of MnMoO4/g-C3N4: (A) XPS full spectrum; （B） C 1s （C） N 1s； （D） O 1s； （E） Mn 2p and （F） Mo 3d spectra

3.2 Electrochemical Performance of Different Electrodes

EIS and CV were employed to characterize the different modified electrodes. In the EIS Nyquist plot, the diameter of the semicircle in the high-frequency region corresponds to the electron transfer resistance (Rct), while the linear portion in the low-frequency region reflects the diffusion-controlled process[40]. As shown in Figure 2A, the Rct of the bare GCE is 345.8 Ω (curve a). After modification with $MnMoO_4$ and g-C_3N_4, the Rct values decrease significantly (curves b and c), indicating accelerated electron transfer at the modified electrodes. The $MnMoO_4$/g-C_3N_4/GCE exhibits an even smaller Rct of 81.7 Ω (curve d), suggesting that the $MnMoO_4$/g-C_3N_4 composite facilitates electron transport more effectively. CV was used to investigate the electrochemical performance of GCE, $MnMoO_4$/GCE, g-C_3N_4/GCE, and $MnMoO_4$/g-C_3N_4/GCE. As depicted in Figure 2B, a pair of distinct redox peaks appears on the bare GCE (curve a). Curves b and c represent the CV curves of g-C_3N_4/GCE and $MnMoO_4$/GCE, respectively. The enhancement of redox peak currents after modification with g-C_3N_4 or $MnMoO_4$ can be attributed to the large specific surface area of g-C_3N_4 and the good electrical conductivity of $MnMoO_4$, both of which facilitate electron transfer between the electrode and the $[Fe(CN)_6]^{3-/4-}$ redox probe. The $MnMoO_4$/g-C_3N_4/GCE exhibits the highest redox peak current (curve d), presumably because g-C_3N_4 significantly improves the dispersion of $MnMoO_4$, and the synergistic effect between $MnMoO_4$ and g-C_3N_4 further accelerates the electron transfer rate.

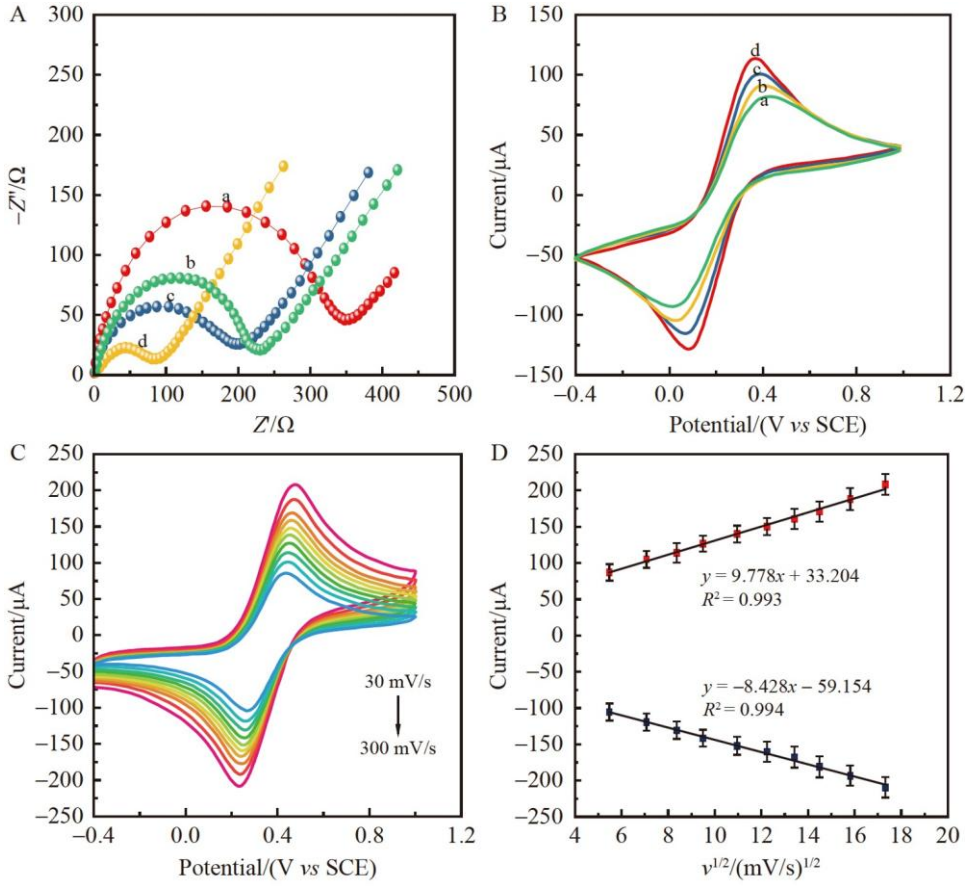

Figure 2 (A) Electrochemical impedance spectroscopy (EIS) and (B) cyclic voltammetry (CV) curves of different electrodes in [Fe(CN)6]3–/4– solution (a: GCE; b: g-C3N4/GCE; c: MnMoO4/GCE; d: MnMoO4/g-C3N4/GCE); (C) CV curves of MnMoO4/g-C3N4/GCE in [Fe(CN)6]3–/4– solution at different scan rates (30–300 mV/s); (D) Linear relationship of square root of scan rate and current

Figure 2C shows the CV curves of $MnMoO_4$/g-C_3N_4/GCE in a solution containing 0.1 mol/L KCl and 5 mmol/L $[Fe(CN)_6]^{3-/4-}$ at different scan rates. As the scan rate increases from 30 to 300 mV/s, the reduction peak current exhibits a good linear relationship with the square root of the scan rate (v1/2) (Rred2 =0.993, Rox2 =0.994) (Figure 2D). This indicates that the electrocatalytic reaction of $[Fe(CN)_6]^{3-/4-}$ on the $MnMoO_4$/g-C_3N_4/GCE is a typical diffusion-controlled process. The Randles-Sevcik equation[41] (Formula 1) was used to calculate the electroactive surface area (A) of the electrode:

$$I_p = 268600n^{3/2}AD^{1/2}Cv^{1/2} \quad (1)$$

where nis the number of electrons transferred, Dis the diffusion coefficient of the redox probe $[Fe(CN)_6]^{3-/4-}$ (6.7×10−6 cm2/s), Cis the concentration of $[Fe(CN)_6]^{3-/4-}$ (5×10−6 mol/cm3), v1/2is the square root of the scan rate, and Ip is the peak current. The calculated electroactive surface areas of the bare GCE and $MnMoO_4$/g-C_3N_4/GCE are approximately 0.0724 and 0.3530 cm^2, respectively. This indicates that the $MnMoO_4$/g-C_3N_4/GCE possesses a high electrochemical active surface area, which favors the enrichment of MNZ on the electrode surface, thereby enhancing the current response.

3.3 Electrochemical Behavior of MNZ on $MnMoO_4$/g-C_3N_4/GCE

Figure 3A presents the CV curves of different electrodes in 0.1 mol/L PBS (pH 7.0) in the absence and presence of 200.0 μmol/L MNZ. In the blank buffer solution, no obvious redox peaks are observed on the bare GCE, $MnMoO_4$/GCE, g-C_3N_4/GCE, or $MnMoO_4$/g-C_3N_4/GCE. Upon addition of MNZ to the PBS, the bare GCE (curve a) exhibits a weak reduction peak current (Ipc =−13.47μA) at −0.58 V.

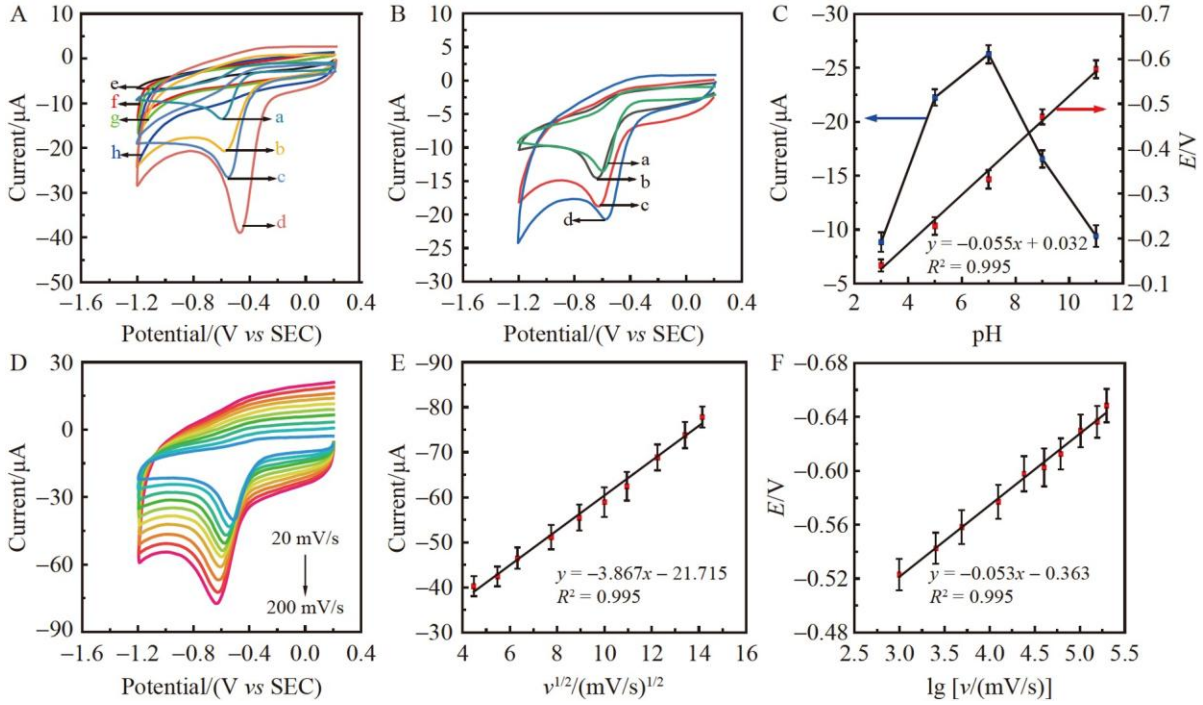

Figure 3 (A) CV curves of different electrodes in PBS solution (0.1 mol/L, pH 7.0) in the absence and presence of 200.0 μmol/L MNZ; (a: GCE+MNZ; b: MnMoO4/GCE+MNZ; c: g-C3N4/GCE+MNZ; d: MnMoO4/g-C3N4/GCE +MNZ; e: GCE; f: MnMoO4/GCE; g: g-C3N4/GCE, h: MnMoO4/g-C3N4/GCE); (B) CV curves of different electrodes (a: GCE; b: MnO2/GCE; c: MoO3/GCE; d: MnMoO4/g-C3N4/GCE) in PBS (pH=7.0) containing 200 μmol/L MNZ at a scan rate of 100 mV/s; (C) Plots of pH vs Ipc and pH vs Epc; (D) CV curves of MnMoO4/g-C3N4/GCE in PBS (pH = 7.0, 200 μmol/L MNZ) at different scan rates; (E) Relationship between square root of scan rate (v1/2) and the peak current (Ipc); (F) Relationship between logarithm of scan rate (lgv) and potentials (Epc)

The Ipc of the $MnMoO_4$/GCE-modified electrode is −20.78 μA (curve b), and that of the g-C_3N_4/GCE-modified electrode is −26.53 μA (curve c). A distinct reduction peak appears on the $MnMoO_4$/g-C_3N_4/GCE (curve d), with an Ipc of −38.95 μA and a peak potential (Epc) of −0.46 V, indicating a favorable electrochemical response of MNZ on the $MnMoO_4$/g-C_3N_4/GCE. This may be attributed to the composite structure of $MnMoO_4$ and g-C_3N_4, which provides higher catalytic activity and a larger specific surface area, thereby accelerating the reduction reaction rate of MNZ[42]. As shown in Figure 3B, compared with the bare GCE, MNZ exhibits a reduction peak at −0.64 V on the MnO_2/GCE, with a peak current of −14.49 μA. On the MoO_3/GCE, the reduction peak of MNZ is located at −0.62 V, with a peak current of −18.63 μA. In contrast, MNZ on the $MnMoO_4$/g-C_3N_4/GCE electrode shows a prominent reduction peak (Ipc=−20.78 μA, Epc=−0.57 V). This could be due to the high oxidation states of molybdenum (Mo) and manganese (Mn) in $MnMoO_4$, which confer good electrochemical activity. Additionally, the unique crystal structure and surface morphology of $MnMoO_4$ likely provide more active sites and a larger specific surface area, thus increasing the efficiency of the reduction reaction.

3.4 Optimization of Experimental Conditions

3.4.1 Effect of Solution pH on the Electrochemical Reaction of MNZ

The effect of pH (ranging from 3.0 to 11.0) of the 0.1 mol/L PBS on the electrochemical behavior of 200 μmol/L MNZ was investigated. From the CV curves in Figure 3C, it is observed that at a scan rate of 100 mV/s, the reduction peak current of MNZ initially increases and then decreases with rising pH, reaching its maximum at pH 7.0. Therefore, pH 7.0 PBS was selected for subsequent experiments. Concurrently, the cathodic peak potential (Epc) shifts negatively throughout the process. The linear relationship between Epc and pH is described by the equation Epc (V)=−0.055x+0.032(R2=0.995). The slope of −0.055 V/pH is close to the Nernstian theoretical value (−59 mV/pH), suggesting that the electrode reaction involves an equal number of electrons and protons[43].

3.4.2 Effect of Scan Rate on the Electrochemical Reaction of MNZ

Figure 3D displays the CV curves of 200 µmol/L MNZ on the $MnMoO_4$/g-C_3N_4/GCE at different scan rates. Within the range of 20–200 mV/s, the peak current increases gradually with the scan rate, while the peak potential shifts negatively. The peak current exhibits a good linear relationship with the square root of the scan rate (Figure 3E), described by the equation Ipc =−3.867v1/2((mV/s)1/2)−21.715(R2=0.995). This confirms that the reaction of MNZ on the $MnMoO_4$/g-C_3N_4/GCE within this scan rate range is a diffusion-controlled process[44]. Furthermore, the peak potential also shows a good linear relationship with the logarithm of the scan rate (Figure 3F), following the equation Epc =−0.053lgv−0.363(R2=0.995). The number of transferred electrons (n) and the electron transfer coefficient (α) were calculated using the Laviron equations[45]:

$$I_C(\mathrm{A}) = -2.99 \times 10^5 n(\alpha n_\alpha)^{1/2} \mathrm{ACD}^{1/2} v^{1/2} \quad (2)$$

$$E_p = E^0 - \frac{RT}{\alpha n_\alpha F}\left[0.78 + \ln\left(\frac{Dox^{1/2}}{K^0}\right) + \ln\left(\frac{\alpha n_\alpha F}{RT}\right)^{1/2}\right] - \frac{RT}{2\alpha n_\alpha F}\ln v \quad (3)$$

In Formula (2), nis the number of electrons transferred during the reduction process, nα is the number of electrons in the rate-determining step, αis the electron transfer coefficient, Ais the electrode surface area (cm^2), Dis the diffusion coefficient (cm^2/s), vis the scan rate (V/s), and Cis the concentration of MNZ (mol/cm^3). In Formula (3), Ep is the peak potential, E0 is the standard potential, Ris the ideal gas constant (8.314 J/(K·mol)), Tis the temperature (K), and Fis the Faraday constant (96485 C/mol). Based on the experimental results, nα=1, indicating that the reaction of MNZ on the $MnMoO_4$/g-C_3N_4/GCE surface involves an equal number of electrons and protons. Combining Formulas (2) and (3), α=0.558, and the calculated nfor MNZ on the $MnMoO_4$/g-C_3N_4/GCE electrode is approximately 4. Accordingly, the possible reaction mechanism of MNZ on the $MnMoO_4$/g-C_3N_4/GCE electrode is proposed in Figure 4. During the reduction process, the MNZ molecule accepts electrons, and the nitro group is reduced to a hydroxylamine group. Functional groups in MNZ (e.g., hydroxyl and amine groups) may form hydrogen bonds with oxygen species or nitrogen atoms on the surface of the $MnMoO_4$/g-C_3N_4 composite, enhancing the adsorption stability of MNZ on the electrode surface. Simultaneously, these functional groups may coordinate with metal ions on the composite surface, facilitating the reduction reaction[46].

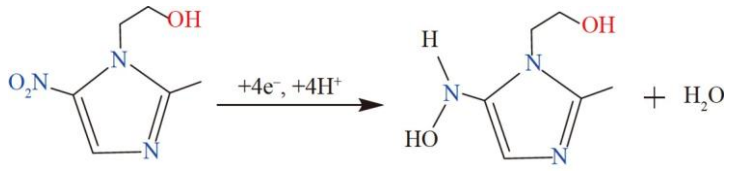

Figure 4 Possible electro-reduction mechanism of MNZ on MnMoO4/g-C3N4/GCE electrode

3.5 Quantitative Detection of MNZ

Under optimized experimental conditions, the electrochemical responses of MNZ at different concentrations on the $MnMoO_4$/g-C_3N_4/GCE were detected using DPV (Figure 5A). The DPV response current of the $MnMoO_4$/g-C_3N_4/GCE exhibits good linear relationships with MNZ concentration in two ranges: 0.5–100 µmol/L and 100–2400 µmol/L (Figure 5B). The linear regression equations are I=−0.163C(µmol/L)−5.279(R2=0.985) and I=−0.017C(µmol/L)−20.276(R2=0.995), respectively. The limit of detection (LOD, 3σ/k) is 1.33 nmol/L. Compared with previously reported electrochemical methods for MNZ detection (Table 1), the proposed method offers a lower detection limit and a wider linear range.

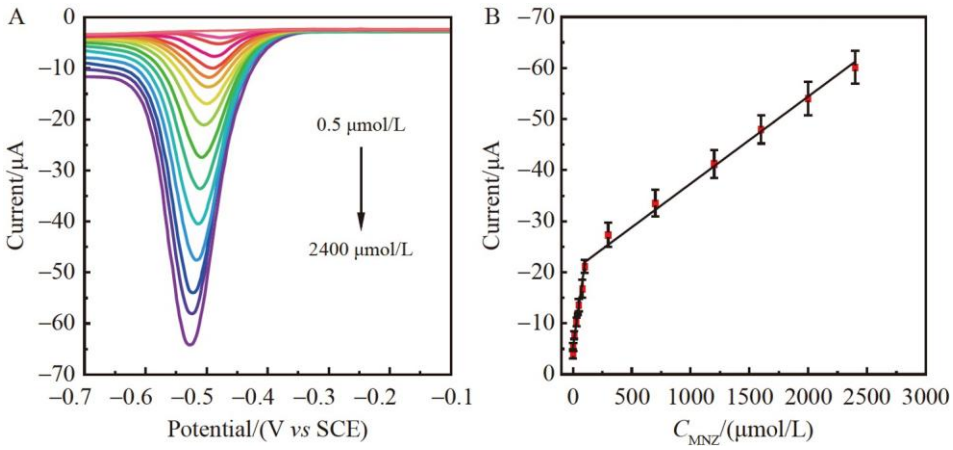

Figure 5 (A) DPV curves of MnMoO4/g-C3N4/GCE in the presence of different concentrations of MNZ in 0.1 mol/L PBS (pH 7.0); (B) Calibration plot of reduction peak current versus MNZ concentration

3.6 Selectivity, Stability, and Reproducibility

To evaluate the selectivity of the $MnMoO_4$/g-C_3N_4/GCE for MNZ detection, the electrochemical response to 200 μmol/L MNZ was measured in the presence of interfering substances, including 200-fold concentrations of uric acid, ascorbic acid, glucose, Ca^{2+}, Fe^{2+}, and nitro compounds (nitrofurantoin (NIT), nitrobenzene (NB), and nifedipine (NF)). As shown in Figure 6A, the presence of these interferents had minimal impact on the sensor's response to MNZ, demonstrating good anti-interference capability and selectivity. Five $MnMoO_4$/g-C_3N_4/GCE electrodes were fabricated independently and used to detect 200 μmol/L MNZ. The results (Figure 6B) yielded a relative standard deviation (RSD) of 0.6%, indicating excellent fabrication reproducibility. After storing the $MnMoO_4$/g-C_3N_4/GCE at room temperature (25 °C) for 30 days, the response current retained 93.0% of its initial value (Figure 6C), confirming the good stability of the electrochemical sensor.

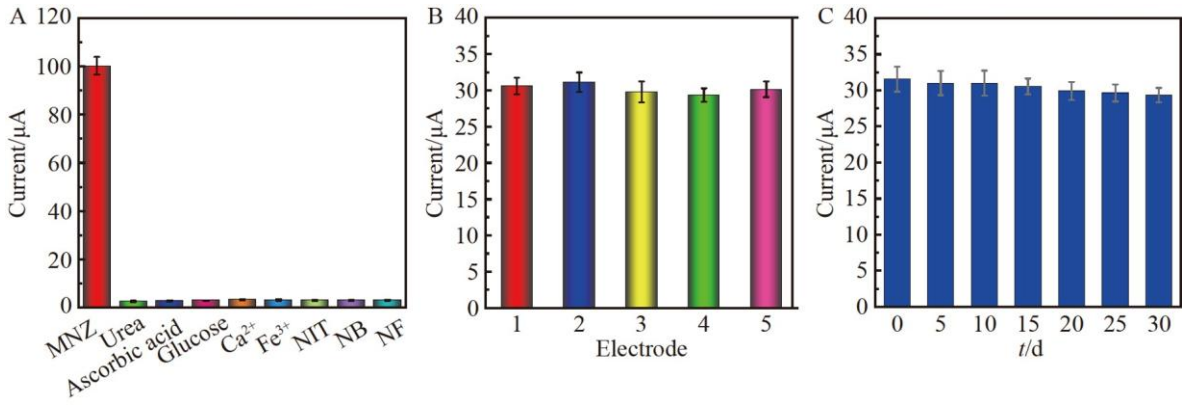

Figure 6 (A) Selectivity, (B) preparation reproducibility and (C) storage stability of MnMoO4/g-C3N4/GCE

Table 1 Comparison of performance for detection of MNZ by different modified electrodes

Electrode materials	Linear range / (μmol/L)	LOD / (nmol/L)	Ref.
O-gCN/GCE	0.01–2060	5.0	[46]
Fe/NC-Nafion/GCE	0.1–100	31	[47]
GR/Fe_3O_4NPs/GCE	0.05–120	0.23	[48]

MIP/$CuCo_2O_4$/N-CNTs/GCE	0.05–100	0.48	[49]
Ag@C/N-rGO/MWCNTs	0.1–150	44.1	[50]
$MnMoO_4$/g-C_3N_4/GCE	0.5–2400	1.33	This work

Note: O-gCN: Oxygen-doped graphitic carbon nitride; Fe/NC: Nanoporous nitrogen-doped carbon nanoparticles decorated with Fe component; GR: Graphene; NPs: Nanoparticles; MIP: Molecularly imprinted polymer; N-CNTs: Nitrogen-doped carbon nanotubes; N-rGO: Nitrogen-doped reduced graphene oxide; MWCNTs: Multi-walled carbon nanotubes.

3.7 Real Sample Analysis

To assess the applicability of the electrochemical sensor in real samples, it was employed to detect MNZ in commercially available egg and milk samples. The results are summarized in Table 2. The spiked recoveries ranged from 97.7% to 103.7% for egg samples and 96.9% to 102.4% for milk samples, with RSDs of 1.1%–2.1% and 1.5%–2.2%, respectively. These findings indicate that the electrochemical sensor possesses good accuracy and practicality for the determination of MNZ in egg and milk samples.

Table 2 Determination results of MNZ in eggs and milk samples

Sample	**Added / (μmol/L)**	**Found / (μmol/L)**	**Recovery / %**	**RSD / (%, n=3)**
Egg	10.00	9.77	97.7	1.1
	50.00	51.87	103.7	1.9
	100.00	98.34	98.3	2.1
Milk	10.00	9.69	96.9	2.1
	50.00	48.67	97.3	2.2
	100.00	102.35	102.4	1.5

4 Conclusion

A novel electrochemical sensor based on a $MnMoO_4$/g-C_3N_4 composite-modified GCE ($MnMoO_4$/g-C_3N_4/GCE) was successfully constructed for the detection of MNZ residues in egg and milk samples. The $MnMoO_4$/g-C_3N_4 composite exhibited rapid electron transfer kinetics and good electrocatalytic activity toward MNZ reduction. Electrochemical testing demonstrated that the $MnMoO_4$/g-C_3N_4-modified electrode possessed a wide linear range (0.5–2400 μmol/L), a low detection limit (1.33 nmol/L), as well as good selectivity, reproducibility, and stability. When applied to the detection of MNZ in egg and milk samples, the spiked recoveries were 97.7%–103.7% and 96.9%–102.4%, respectively. This study provides a novel and efficient method for the rapid detection of MNZ in food products.

References

[1] FARID N F, ABDELWAHAB N S. Microchem. J., 2022, 183: 108048.
[2] VASSEGHIAN Y, DRAGOI E N, ALMOMANI F, LE V T. Chemosphere, 2022, 286: 131727.
[3] VERWIJS M C, AGABA S K, DARBY A C. Am. J. Obstet. Gynecol., 2020, 222(2): 157.e1-157.e13.
[4] CERUELOS A H, ROMERO-QUEZADA L C, LEDEZMA J C R, CONTRERAS L L. Eur. Rev. Med. Pharmacol. Sci., 2019, 23(1): 397-401.

[5] GB 31650-2019. National Food Safety Standard—Maximum Residue Limit for Veterinary Drugs in Food. N ational Standards of the People's Republic of China.
[6] ZHONG C, CHEN B, HE M, HU B. J. Chromatogr. A, 2017, 1483: 40-47.
[7] VANOL P G, SANYAL M, SHAH P A, SHRIVASTAV P S. Biomed. Chromatogr., 2018, 32(8): e4242.
[8] SHI S, YU H, YANG F, YAO W, XIE Y. Food Biosci., 2022, 48: 101755.
[9] LIU M X, YIN J H, MENG L, XU N. Chin. J. Anal. Chem., 2020, 48(11): 1556-1563.
[10] AYANKOJO A G, REUT J, OPIK A, SYRITSKI V. Sens. Actuators, B, 2020, 320: 128600.
[11] UMAPATHI R, GHOREISHIAN S M, SONWAL S, RANI G M, HUH Y S. Coord. Chem. Rev., 2022, 453: 214305.
[12] ARUMUGAM B, MUTHUKUTTY B, CHEN S M, RAMARAJ S K, VINOTH KUMAR J V, NAGARAJAN E R. Ultraso n. Sonochem., 2020, 66: 104977.
[13] HUANG T, ZHAO C, QIU Z, LUO J, HU Z. Ionics, 2017, 23(1): 139-146.
[14] RAJAKUMARAN R, RAMKI S, CHEN S M, CHEN T W, VEERASANKAR S, TSENG T W, HUANG C C. Int. J. Electr ochem. Sci., 2019, 14(7): 6571-6585.
[15] NAMVAR F, BESHKAR F, SALAVATI-NIASARI M. J. Mater. Sci.: Mater. Electron., 2017, 28(11): 7962-7968.
[16] SELVI S V, RAJAJI U, CHEN S M, JEBARANJITHAM J N. Colloids Surf., A, 2021, 631: 127733.
[17] ZHANG Y, ZHANG W, WANG X H, MA P Y, SUN Y, SONG D Q. Chin. J. Anal. Chem., 2022, 50(1): 64-72.
[18] ZHANG L, LI X Q, WANG G L. Chin. J. Anal. Chem., 2020, 48(6): 703-711.
[19] SEKAR K, RAJI G, CHEN S, LIU S, XING R. Appl. Surf. Sci., 2020, 527: 146856.
[20] GURU S, KUMAR S, BELLAMKONDA S, GANGAVARAPU R R. Int. J. Hydrogen Energy, 2021, 46(30): 16414-1 6430.
[21] YIN H Y, ZHENG Y F, WANG L. J. Nanosci. Nanotechnol., 2020, 20(9): 5539-5545.
[22] ZHAO P, HUANG L, WANG H, WANG C, CHEN J, YANG P, NI M. Sens. Actuators, B, 2022, 350: 130853.
[23] LIAO X, WANG X, MA C, ZHANG L, ZHAO C, CHEN S, LI K, ZHANG M, MEI L, QI Y, HONG C. Bioelectrochemis try, 2021, 142: 107931.
[24] GUO R, WANG J, BI Z, CHEN X, HU X, PAN W. Chemosphere, 2022, 295: 133834.
[25] JIANG W, LUO W, WANG J, ZHANG M, ZHU Y. J. Photochem. Photobiol., C, 2016, 28: 87-115.
[26] ANUPRIYA J, RAJAKUMARAN R, CHEN S M, KARTHIK R, KUMAR J V, SHIM J J, SHAFI P M, LEE J W. Chemosp here, 2022, 296: 133997.
[27] AHMAD K, RAZA W, ALSULMI A, KIM H. Diamond Relat. Mater., 2023, 138: 110178.
[28] [28] LIU R, HAN X, LIU R, SUN Y. Mater. Lett., 2022, 325: 132811.
[29] APPIAGYEI A B, ASIEDUA-AHENKORAH L, BATHULA C, KIM H S, HAN S S, RAO K M, ANANG D A. J. Energy St orage, 2023, 58: 106383.
[30] ZHANG L, BAI J, GAO F, LI S, LIU Y, GUO S. J. Alloys Compd., 2022, 906: 164394.
[31] ZHANG J, HOU Q, CHANG J, ZHANG D, PENG Y, YANG X. Solid State Sci., 2021, 121: 106750.
[32] LIU W, WANG M, XU C, CHEN S. Chem. Eng. J., 2012, 209: 386-393.
[33] WANG H, XIE A, LI S, WANG J, CHEN K, SU Z, SONG N, LUO S. Anal. Chim. Acta, 2022, 1211: 339907.
[34] PRATIBHA J, RAJPUT J K. J. Electroanal. Chem., 2020, 878: 114605.
[35] VENKATESH K, RAJAKUMARAN R, CHEN S M, KARUPPIAH C, YANG C C, RAMARAJ S K, ALI M A, AL-HEMAID F M A, EL-SHIKH M S, ALMUNQEDHI B M A. Chemosphere, 2021, 273: 129665.
[36] RANJITH K S, EZHIL VILIAN A T, GHOREISHIAN S M, UMAPATHI R, HWANG S K, OH C W, HUH Y S, HAN Y K. J. Hazard. Mater., 2022, 421: 126775.
[37] GAO L, MA Y, ZHANG C, CAO M. J. Alloys Compd., 2023, 968: 172008.
[38] WEI H, YANG J, ZHANG Y, QIAN Y, GENG H. J. Colloid Interface Sci., 2018, 524: 256-262.
[39] CAO H, WU N, LIU Y, WANG S, DU W, LIU J. Electrochim. Acta, 2017, 225: 605-613.
[40] VILIAN A T E, RANJITH K S, LEE S J, UMAPATHI R, HWANG S K, OH C W, HUH Y S, HAN Y K. Electrochim. Act a, 2020, 354: 136723.
[41] XHAKAZA N M, CHOKKAREDDY R, REDHI G G. J. Mol. Liq., 2022, 368: 120444.
[42] THANGAPPAN R, DHINESH KUMAR R, JAYAVEL R. J. Energy Storage, 2020, 27: 101069.
[43] LIANG C Y, LIU F P, ZHANG C Z, ZHANG Z F, WEI Y L, PENG J Y. Chin. J. Anal. Chem., 2019, 47(5): 739-747.
[44] VAN RYSSELBERGHE P. J. Am. Chem. Soc., 1955, 77(8): 2349-2350.
[45] LAVIRON E. J. Electroanal. Chem., 1979, 101(1): 19-28.
[46] KESAVAN G, VINOTHKUMAR V, CHEN S M, THANGADURAI T D. Appl. Surf. Sci., 2021, 556: 149814.
[47] BAIKELI Y, MAMAT X, HE F, XIN X, LI Y, AISA H A, HU G. Ecotoxicol. Environ. Saf., 2020, 204: 111066.
[48] ZOKHTAREH R, RAHIMNEJAD M, NAJAFPOUR-DARZI G, KARIMI-MALEH H. Environ. Res., 2023, 216: 11464 3.

[49] WANG Y, YAO L, LIU X, CHENG J, LIU W, LIU T, SUN M, ZHAO L, DING F, LU Z, ZOU P, WANG X, ZHAO Q, RAO H. Biosens. Bioelectron., 2019, 142: 111483.
[50] LI Y, CHEN R X. Chem. Reagents, 2021, 43(6): 718